Appl. Phys. B (2017) 123:115
DOI 10.1007/s00340-017-6696-9

Applied Physics B
Lasers and Optics

RAPID COMMUNICATION

Multi-band metamirrors for linear to circular polarization conversion with wideband and wide-angle performances

M. Fartookzadeh[1]

Received: 12 November 2016 / Accepted: 7 March 2017 / Published online: 28 March 2017

Abstract Multi-band operation of the elements of electromagnetic systems can result in merging multiple systems and cost reduction. A challenge for multi-band operation is the circular polarization which is frequently a requirement for these systems. However, circular polarization can be obtained from linearly polarized waves using transmission-mode or reflection-mode linear to circular polarization converters. Therefore, advanced multi-band reflection-mode linear to circular polarization converters are proposed in this paper. Two versions of the polarizers are designed with different design methodologies. The first polarization converter has 3 dB axial ratio bandwidths of 29.3, 21.8, and 7.6% on 2, 8, and 12 GHz with 15° permitted incident angle difference. The second polarization converter with incident angle range of 25° ($\theta_{min} = 23°$ and $\theta_{max} = 48°$) has 17.8, 10, and 22.5% bandwidths on 2, 5.5, and 8 GHz, respectively. In addition, the bandwidths can be improved to 32.1, 28.3, and 26.5% by reducing the incident angle range to 10° with $\theta_{min} = 30°$ and $\theta_{max} = 40°$. Finally, a prototype of the second polarization converter is fabricated and simulations are met by measurement results.

1 Introduction

Metamaterials are periodic structures with various shapes to obtain certain functionalities such as polarization conversion [1–6], wave absorption [7–12], and negative refraction [13–16] at desired frequencies. A notable application of metamaterials is the conversion of linearly polarized electromagnetic wave to circular polarization (CP) in the range of microwave to optical frequencies. Although realization technologies of these metamaterials are completely dissimilar for different frequencies, principles of operations, design techniques, and simulation methods are almost similar [1–6]. A characteristic for circularly polarized electromagnetic wave is that the wave with right-hand circular polarization (RHCP) is usually reflected with left-hand circular polarization (LHCP) from a target. In addition, radar and imaging systems generally involve transmitted and received waves those should be separated in their antenna sections. Therefore, a key method for the separation of transmitted and received waves is to use circular polarization. Furthermore, circularly polarized receivers are widely spread in all electromagnetic wave applications. Radar systems, earth stations, scanners, and satellite systems are examples of these applications.

CP can be obtained from the circularly polarized antenna elements using regular methods such as multi-feed antennas, helical antennas, and spiral antennas. [17–20]. Another method is the sequential rotation technique that produces the CP from the array of linearly polarized antennas with unique angular and phase arrangements [21–24]. Reflection-mode linear to circular polarization converters (RMCPs) and transmission-mode linear to circular polarization converters (TMCP) based on metamaterials are alternative methods to produce CP from linearly polarized waves. Operating methods of most of TMCPs are similar. They usually provide 90° phase difference between TE and TM waves of an incident wave to produce the outgoing wave with CP. A simple method is to provide a condition that the TE and TM waves have different phase speeds. For example, parallel conductive plates and parallel dielectrics use this method [1]. Another method is to construct

✉ M. Fartookzadeh
Mahdi.fartookzadeh@gmail.com

[1] Department of Electrical and Electronics Engineering, Malek Ashtar University, P. O. Box 1774-15875, Tehran, Iran

a structure with different equivalent transmission line circuits for TE and TM modes that produces 90° phase difference between TE and TM transmissions. Examples of this method are patch and lines, and meandered lines [1].

RMCPs use similar methods, only they should produce 90° phase difference between TE and TM reflections instead of the transmissions. Viable examples are helical structures on a surface [25] and dipole array structures [26]. Polarization converters have some advantages over the previous methods, and they are now essential in many electromagnetics applications [1]. However, they are affected by limited bandwidth; hence, the bandwidth improvement is of major interest in the literature [25, 27]. Also, dual-band and multi-band polarization converters can improve the applications of electromagnetic systems significantly [28–32].

In many electromagnetic systems, the main limitation of bandwidth of total system is on the 3 dB axial ratio (AR) bandwidth. Moreover, all features of these systems are typically able to have multi-band operations excepting AR which is the main limitation. Thus, multi-band linear to circular polarization converters can improve the performance of these systems, significantly. In addition, the RMCP can be used for many electromagnetic systems such as imaging and radar systems [33, 34]. However, among various available structures for RMCPs [1, 25–32, 35], an RMCP with multi-band, wideband, and wide-angle capabilities together are not reported yet. Bandwidth is very important for practical applications since the bandwidth improvement improves the fabrication tolerances and enables the use of wideband signals. In addition, wide-angle feature makes possible the employment of wide-beam antennas in real applications.

Consequently, multi-band RMCPs with wideband and wide-angle advantages are proposed in this paper. The proposed multi-band metamaterial RMCPs are based on two design methods. The first one based on equivalent transmission line circuit with 15° permitted incident angle difference has 29.3, 21.8, and 7.6% bandwidths on 2, 8, and 12 GHz, and the second one is designed to reduce the distances between operating frequencies using simulation optimizations. The bandwidths of second metamaterial are 17.8, 10, and 22.5% at 2, 5.5 and 8 GHz, with $\theta_{\min} = 23°$ and $\theta_{\max} = 48°$. Also, the bandwidths can be improved to 32.1, 28.3, and 26.5% by reducing the incident angle difference to 10°. Finally, simulations are validated by measured results and good agreements are observed.

2 Multi-band RMCP based on equivalent transmission line circuit

The proposed RMCPs are based on dual-layer patch arrays similar to the dual-band RMCP [35]. Two methods are proposed for constructing multi-band RMCPs; the first method uses the equivalent transmission line circuit to obtain the dimensions, and the second method obtains the dimensions using simulation optimizations. The second RMCP has wider angle of incidence range and its operating frequencies are closer to each other which is an advantage. However, the initial structure is obtained using the analytical method and then by violating the limitations of this method, the results are improved as will be indicated in next section.

The design approach is similar with the dual-band dual-layer RMCP using the equivalent transmission line circuit as indicated in Fig. 1a. Dual-layer RMCPs have indeed TE and TM equivalent transmission line circuit models; however, the circuit models are similar and only values of the components Y_0, Y_1, Y_2, Y_{s1} and Y_{s2} are different. The substrate width is 3.2 mm and $\epsilon_r = 3.9$. Patch sizes are obtained by matching the calculated TE susceptance of the first layer patches with required susceptance

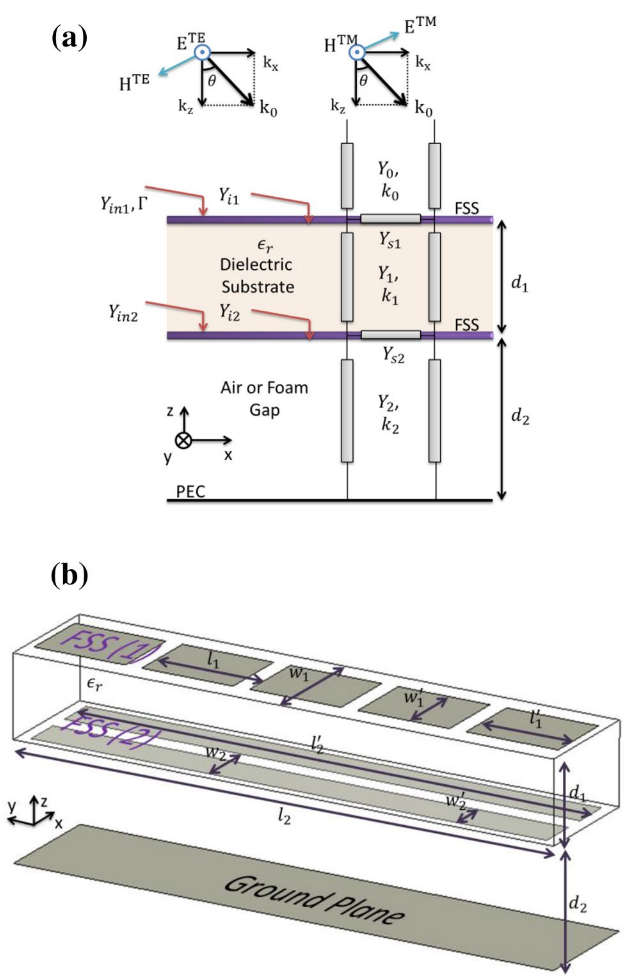

Fig. 1 **a** Equivalent transmission line circuit for dual-layer RMCPs and **b** unit cell of the proposed dual-layer RMCP based on patch arrays

at the desired frequencies for CP. The detailed analytical method is available in [26, 35, 36] and only brief explanations are provided here. The $\hat{x}$ component of propagation constant, k_x, is unique in Fig. 1a and equals $k_0 \sin\theta$ in all layers due to the boundary conditions and $k_{z\iota} = \sqrt{k_\iota^2 - k_x^2}$ for ιth th layer, where $k_\iota = \sqrt{\epsilon_{r\iota}}k_0$. Characteristic impedances of the ιth th layer for TE and TM modes are $Y_\iota^{\mathrm{TM}} = \omega\epsilon_0\epsilon_{r\iota}/k_{z\iota}$ and $Y_\iota^{\mathrm{TE}} = k_{z\iota}/\omega\mu_0$, with $\epsilon_{r0} \cong \epsilon_{r2} \cong 1$ and the relative permittivity of substrate is $\epsilon_{r1} = 3.9$. The reflection coefficients, for 45° polarization angle of the incident wave, should meet $\Gamma^{\mathrm{TE}} = \mp j\Gamma^{\mathrm{TM}}$ for RHCP and LHCP reflection, where $\Gamma = (Y_0 - Y_{\mathrm{in}})/(Y_0 + Y_{\mathrm{in}})$ for both TE and TM waves [36]. $Y_{\mathrm{i1}}^{\mathrm{TM}}$ and $Y_{\mathrm{i1}}^{\mathrm{TE}}$ are TM and TE input admittances of circuit without considering $Y_{\mathrm{s1}}^{\mathrm{TM}}$ and $Y_{\mathrm{s1}}^{\mathrm{TE}}$. Input admittances are therefore $Y_{\mathrm{in1}} = Y_{\mathrm{i1}} + Y_{\mathrm{s1}}$ for both TE and TM modes. Consequently, required admittance for the patch array of the first layer is [26]

$$Y_{\mathrm{s1,req}}^{\mathrm{TE}} = jB_{\mathrm{s1,req}}^{\mathrm{TE}} = j\left[\frac{-j\left(Y_{\mathrm{i1}}^{\mathrm{TM}} + Y_{\mathrm{s1}}^{\mathrm{TM}}\right) \pm Y_0^{\mathrm{TM}}}{Y_0^{\mathrm{TM}} \pm j\left(Y_{\mathrm{i1}}^{\mathrm{TM}} + Y_{\mathrm{s1}}^{\mathrm{TM}}\right)} Y_0^{\mathrm{TE}} + jY_{\mathrm{i1}}^{\mathrm{TE}}\right], \tag{1}$$

where the admittances $Y_{\mathrm{i1}}^{\mathrm{TM}}$, $Y_{\mathrm{i1}}^{\mathrm{TE}}$ and $Y_{\mathrm{s1}}^{\mathrm{TM}}$ are pure imaginary for negligible losses. Using equivalent transmission line circuit in Fig. 1a for both TE and TM modes, one obtains [36]

$$Y_{\mathrm{i1}} = jB_{\mathrm{i1}} = Y_1 \frac{Y_{\mathrm{in2}} + jY_1 \tan\left(k_{z1}d_1\right)}{Y_1 + jY_{\mathrm{in2}} \tan\left(k_{z1}d_1\right)},$$

where Y_{in2} is the input admittance of second layer. Y_{i1} can be obtained by substituting $Y_{\mathrm{in2}} = Y_{\mathrm{i2}} + Y_{\mathrm{s2}} = Y_{\mathrm{s2}} - jY_2 \cot\left(k_{z2}d_2\right)$ in this equation as

$$Y_{\mathrm{i1}} = jB_{\mathrm{i1}} = jY_1 \frac{-jY_{\mathrm{s2}} + Y_1 \tan\left(k_{z1}d_1\right) - Y_2 \cot\left(k_{z2}d_2\right)}{Y_1 + \left[jY_{\mathrm{s2}} + Y_2 \cot\left(k_{z2}d_2\right)\right] \tan\left(k_{z1}d_1\right)}, \tag{2}$$

for both TE and TM situations. $Y_{\mathrm{s1}}^{\mathrm{TM}}$, $Y_{\mathrm{s2}}^{\mathrm{TM}}$ and $Y_{\mathrm{s2}}^{\mathrm{TE}}$ are dependent on shapes of the frequency-selective surfaces (FSSs) in (1) and (2). Unit cell of the proposed RMCP is indicated in Fig. 1b. The TM and TE surface admittances of ιth layer ($\iota = 1, 2$) are given by [37]

$$Y_{\mathrm{s}\iota}^{\mathrm{TM}} = -j\left(\frac{2\omega\mu_0 w_\iota}{\pi\eta_{\mathrm{eff}}^2}\right) \ln\left(\cos\frac{\pi w'_\iota}{2w_\iota}\right) \tag{3}$$

and

$$Y_{\mathrm{s}\iota}^{\mathrm{TE}} = -j\left(\frac{2\omega\mu_0 l_\iota}{\pi\eta_{\mathrm{eff}}^2}\right) \ln\left(\cos\frac{\pi l'_\iota}{2l_\iota}\right)\left(1 - \frac{\sin^2\theta}{2\epsilon_{\mathrm{eff}}}\right), \tag{4}$$

respectively, where $\epsilon_{\mathrm{eff}} \cong (\epsilon_r + 1)/2$ and $\eta_{\mathrm{eff}} = \sqrt{\mu_0/\epsilon_0\epsilon_{\mathrm{eff}}}$. Equations (3) and (4) are lines that pass from the origin as functions of frequency. Consequently, dimensions should be tuned to obtain a $B_{\mathrm{s1,req}}^{\mathrm{TE}}$ curve that can be connected by a straight line from the origin at desired frequencies. Slope of the $B_{\mathrm{s1}}^{\mathrm{TE}}$ line can be controlled by the dimensions l_1 and l'_1. Required and calculated TE susceptances of the first layer patches for CP reflection are indicated in Fig. 2 with the given dimensions at $\theta = 40°$. It can be observed that the required and calculated TE susceptances meet at on 1.3, 2, 8, and 12 GHz. In addition, it can be observed in Fig. 3 that the simulated structure has zero AR at the same frequencies. CST frequency domain solver is used for all simulations. The dimensions are almost similar, only l'_2, w'_2 and l'_1 are slightly changed to compensate the coupling effects, which is not considered in the equivalent transmission line circuit. The first and third frequencies are for RHCP, and the second and fourth frequencies are for LHCP. Polarizations of the reflected wave can be changed by changing the polarization of incident wave from 45° to 135°, explicitly. However, bandwidth of the first operating frequency is low, and therefore, it is not considered. Therefore, it can be observed that this RMCP has 15° permitted incident angle

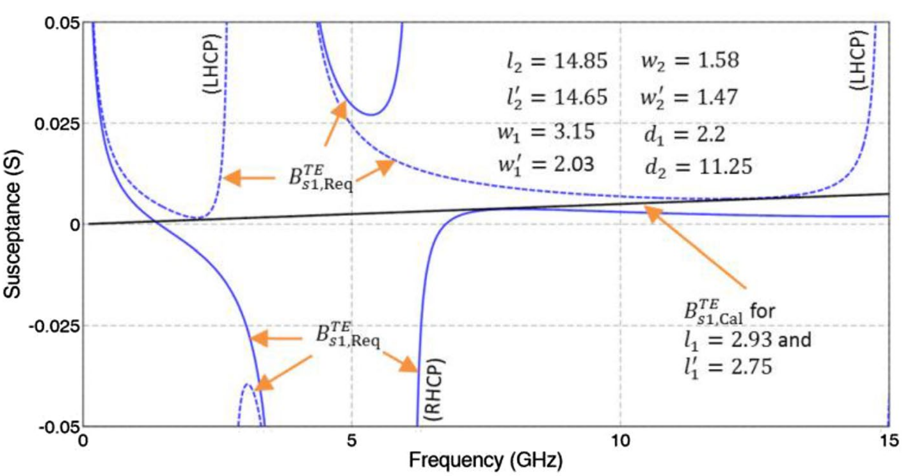

Fig. 2 Required and calculated TE susceptances of the first layer patches for CP reflection for the proposed RMCP in Fig. 1 with given dimensions at $\theta = 40°$ (dimensions in mm)

Fig. 3 Simulated AR of the reflected wave from dual-layer RMCP with dimensions $l_2 = 14.85$, $l_2' = 14.63$, $w_2 = 1.58$, $w_2' = 1.37$, $d_1 = 2.2$, $d_2 = 11.25$, $l_1 = 2.93$, $l_1' = 2.79$, $w_1 = 3.15$, and $w_1' = 2.03$ (all in mm)

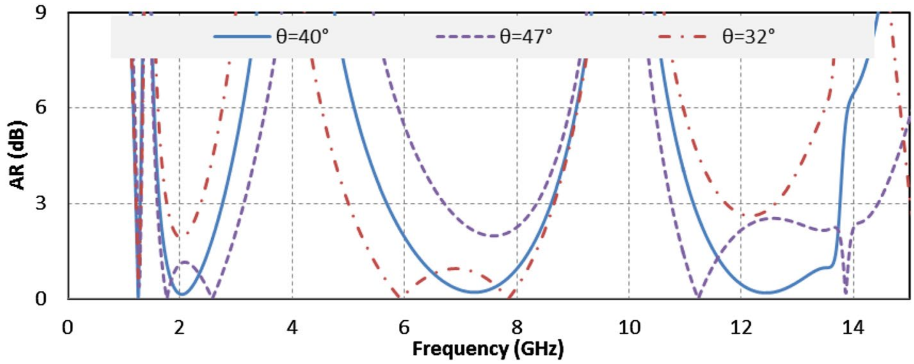

difference with 29.3, 21.8, and 7.6% bandwidths on 2, 8, and 12 GHz.

3 Multi-band RMCP violating limits of equivalent transmission line circuit

Large distances between three frequencies reduce the practical application in multi-band systems, as the realization of other components will be problematic. This is due to large distances between the wavelengths which yield to large differences in dimensions of the components. In addition, in practical multi-band applications, the frequencies are usually closer [38, 39]. Consequently, the dimensions of RMCP with similar structure as indicated in Fig. 1 are optimized to obtain the third frequency band between 2 and 8 GHz. This is actually obtained by violating limitations of the previously introduced equivalent transmission line circuit method, consciously. It means that the dimensions are purposely assumed outside the tolerance of theory so that the coupling effects change the susceptances at lower frequencies as will be indicated shortly.

Dimensions of the second RMCP based on simulation optimizations are $l_2 = 33$, $l_2' = 31$, $w_2 = 3.5$, $w_2' = 3.05$, $d_1 = 3.2$, $d_2 = 8$, $l_1 = 6.6$, $l_1' = 3$, $w_1 = 7$, and $w_1' = 6.2$ (all in mm). AR of the reflected wave from this RMCP is indicated in Fig. 4 for different incident angles. It can be observed that the three operating frequencies are about 2, 5.5, and 8 GHz. These frequencies can be used for satellite applications. The incident angle range is assumed to be 25° with $\theta_{\min} = 23°$ and $\theta_{max} = 48°$. Therefore, the minimum 3 dB AR bandwidths for 2, 5.5, and 8 GHz are 17.8, 10, and 22.5%, respectively. Also, the interesting point is the wide bandwidths at 8 GHz in all angles of the incident wave. However, for other frequencies, the bandwidths can be improved by reducing the range of incident angle to 10° with $\theta_{min} = 30°$ and $\theta_{\max} = 40°$, which yields to the 32.1, 28.3, and 26.5% bandwidths.

Nevertheless, simulation results in Fig. 4 are in agreement with the results of equivalent transmission line circuit for higher than 8.5 GHz as can be observed in Fig. 5. However, the results will be in agreement for less than 5.5 GHz, if l_1' is increased to 6 mm. For the frequencies between 5.5 and 8.5 GHz, the susceptance of this RMCP is corresponding to the values for l_1' between 3 and 6 mm. Therefore, limitations of the equivalent transmission line circuit are violated for lower frequencies where the wavelengths are larger and coupling effects are stronger to obtain the desired results.

In addition, operating frequencies of this RMCP appear to be controllable by changing separation between the ground plane and the second layer FSS. It can be observed in Fig. 6 that by reducing d_2 the frequencies are closer, and the required propagation angle is smaller. This can be better

Fig. 4 Simulated AR of the reflected wave from dual-layer RMCP with dimensions $l_2 = 33$, $l_2' = 31$, $w_1 = 7$, $w_1' = 6.2$, $w_2 = 3.5$, $w_2' = 3.05$, $d_1 = 3.2$, $d_2 = 8$, $l_1 = 6.6$, and $l_1' = 3$ (all in mm)

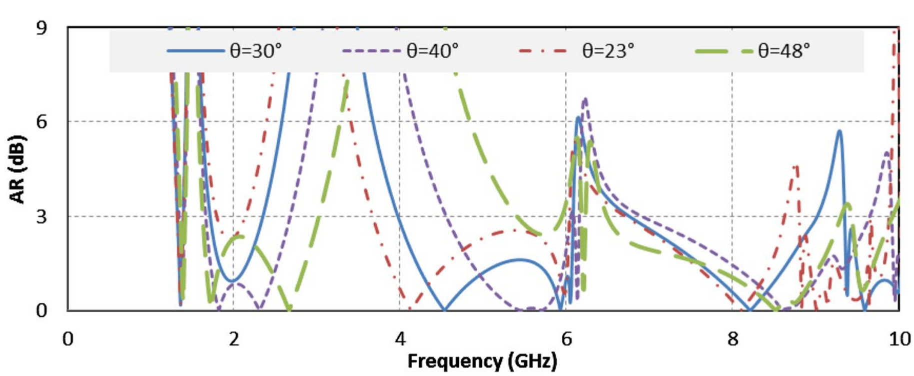

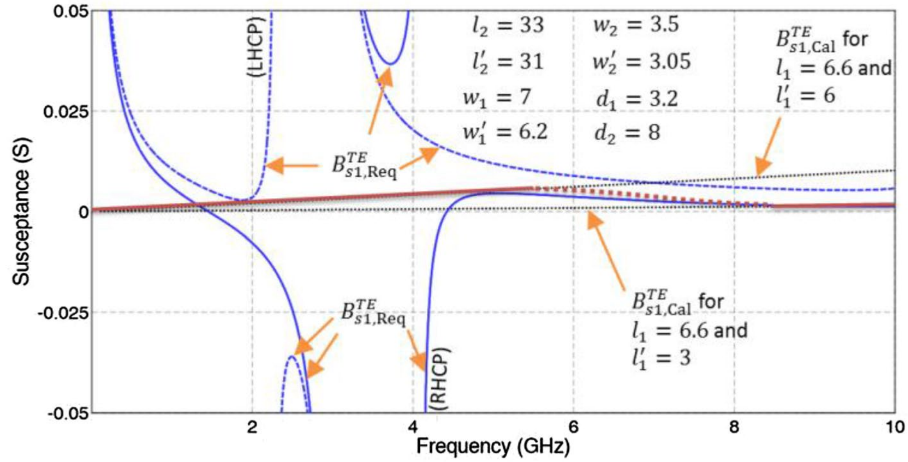

Fig. 5 Required and calculated TE susceptances of the first layer patches for CP reflection for the proposed RMCP in Fig. 1 with given dimensions at $\theta = 40°$ (dimensions in mm); actual behavior of the susceptance for $l'_1 = 3$ mm is also indicated

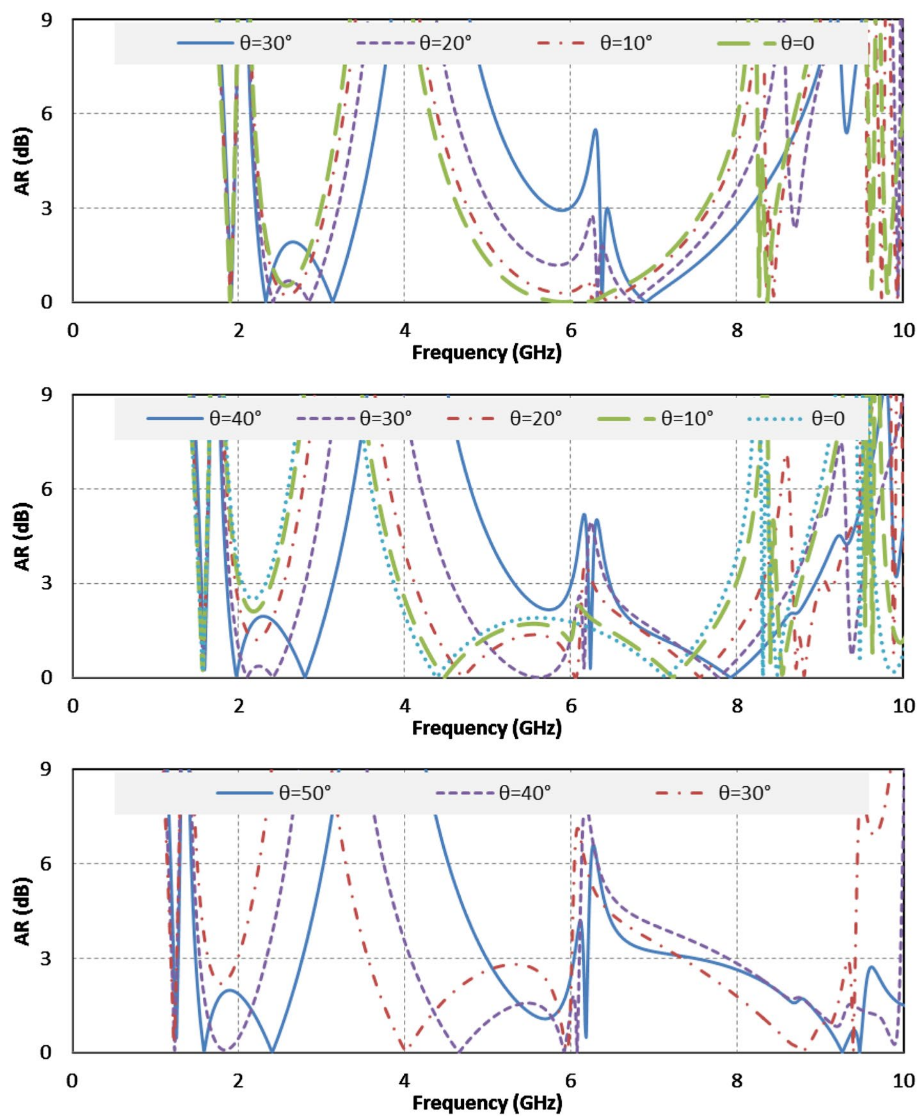

Fig. 6 Effects of changing d_2 on AR of the reflected wave from dual-layer RMCP; dimensions are similar to the dimensions in Fig. 5 only d_2 is changed to 4, 6, and 10 mm, respectively

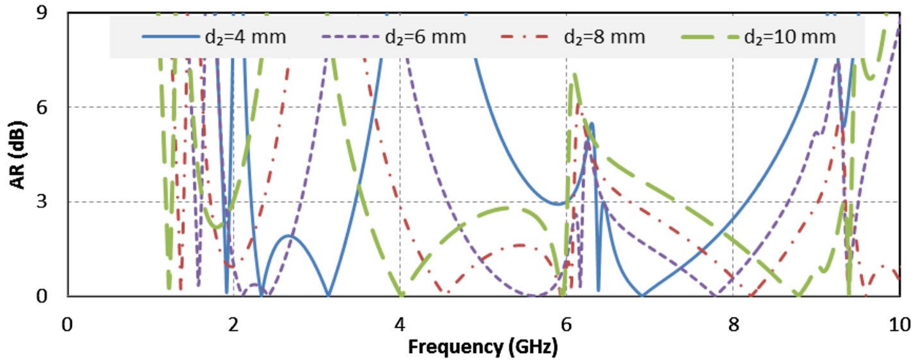

Fig. 7 AR of the reflected wave from dual-layer RMCP with different values of d_2 at $\theta = 30°$

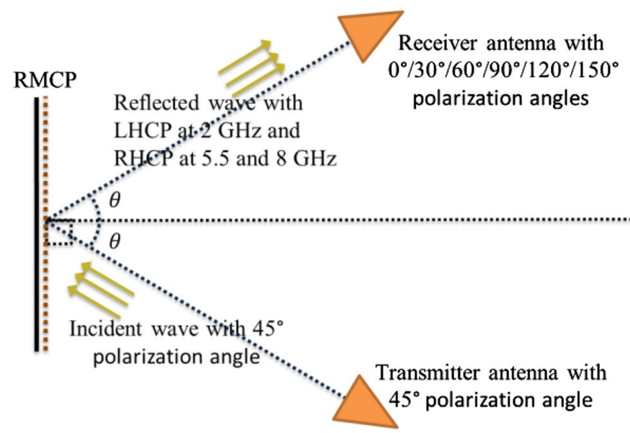

Fig. 8 Schematic of the measurement setup of the proposed RMCP

observed in Fig. 7 where ARs of the reflected wave are indicated at $\theta = 30°$ for the RMCPs with different values of d_2.

Schematic of the measurement setup for the proposed RMCP is indicated in Fig. 8. The propagation angle of incident wave, θ, is 40°, and the polarization angle of the transmitter is 45°. AR is obtained by rotating the receiver antenna and recording the ratio between maximum and minimum received powers at all rotation angles in a given frequency. Photograph of a 35 cm × 30 cm prototype and the measured AR of reflected wave are indicated in Fig. 9. Rectangular patches of the proposed RMCP are printed on both sides of a substrate with 3.2 mm thickness and $\epsilon_r = 3.9$. The substrate is separated 8 mm from the ground plane using pieces of foams. Measurement is achieved using three sets of horn antennas for the frequency ranges 1.8–3 GHz, 3.9–6 GHz, and 6.9–10 GHz. Two antennas are used for each frequency band: one for transmitter with 45° polarization angle and the other for receiver with different polarization angles as indicated in Fig. 8. The measured AR in Fig. 9, which is obtained from the ratio between maximum and minimum received powers at all rotation angles, indicates good agreements with simulated AR.

4 Conclusions

In this paper, multi-band RMCPs are proposed which can help improve the performance and reduce the costs in electromagnetic systems, significantly. Two methods are presented for designing these polarization converters. The first method, based on equivalent transmission line circuit, formed a polarization converter with 3 dB AR bandwidths of 29.3, 21.8, and 7.6% on 2, 8, and 12 GHz, respectively, and the 15° permitted incident angle difference. The second

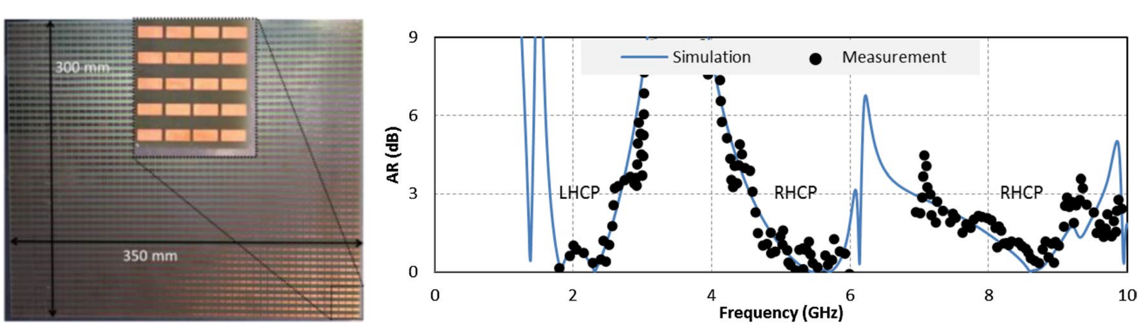

Fig. 9 Realized multi-band RMCP and the measured AR of the reflected wave with $d_2 = 8$ mm at $\theta = 40°$

method, violating the equivalent transmission line circuit limits, made a polarization converter with total incident angle range of 25° ($\theta_{\min} = 23°$ and $\theta_{\max} = 48°$) and 17.8, 10, and 22.5% bandwidths on 2, 5.5, and 8 GHz, respectively. Finally, the second polarization converter is fabricated and tested successfully.

References

1. R.J. Mailloux, *Phased Array Antenna Handbook*. (Artech House, Boston, 2005)
2. J. Zhao, Y. Cheng, A high-efficiency and broadband reflective 90° linear polarization rotator based on anisotropic metamaterial. Appl. Phys. B **122**(10), 255 (2016)
3. Z. Wei, Y. Cao, Y. Fan, X. Yu, H. Li, Broadband polarization transformation via enhanced asymmetric transmission through arrays of twisted complementary split-ring resonators. Appl. Phys. Lett. **99**(22), 221907 (2011)
4. D.L. Markovich, A. Andryieuski, M. Zalkovskij, R. Malureanu, A.V. Lavrinenko, Metamaterial polarization converter analysis: limits of performance. Appl. Phys. B **112**(2)), 143–152 (2013)
5. D. Liu et al., Broadband asymmetric transmission and multi-band 90° polarization rotator of linearly polarized wave based on multi-layered metamaterial. Opt. Commun. **354**, 272–276 (2015)
6. J. Shi, X. Liu, S. Yu, T. Lv, Z. Zhu, H. Feng Ma, T. Jun Cui, Dual-band asymmetric transmission of linear polarization in bilayered chiral metamaterial. Appl. Phys. Lett. **102**(19), 191905 (2013)
7. H. Tao, C.M. Bingham, A.C. Strikwerda, D. Pilon, D. Shrekenhamer, N.I. Landy, K. Fan, X. Zhang, W.J. Padilla, R.D. Averitt, Highly flexible wide angle of incidence terahertz metamaterial absorber: design, fabrication, and characterization. Phys. Rev. B **78**(24), 241103 (2008)
8. H. Tao, C.M. Bingham, D. Pilon, K. Fan, A.C. Strikwerda, D. Shrekenhamer, W.J. Padilla, X. Zhang, R.D. Averitt, A dual band terahertz metamaterial absorber. J. Phys. D Appl. Phys. **43**(22), 225102 (2010)
9. Y. Fan, Z. Liu, F. Zhang, Q. Zhao, Z. Wei, F. Quanhong, L. Junjie, G. Changzhi, L. Hongqiang, Tunable mid-infrared coherent perfect absorption in a graphene meta-surface. Sci. Rep. **5**, 13956 (2015)
10. N. Liu, M. Mesch, T. Weiss, M. Hentschel, H. Giessen, Infrared perfect absorber and its application as plasmonic sensor. Nano Lett. **10**(7), 2342–2348 (2010)
11. Y. Fan, N.-H. Shen, T. Koschny, C.M. Soukoulis, Tunable terahertz meta-surface with graphene cut-wires. ACS Photonics **2**(1), 151–156 (2015)
12. N. Zhang, P. Zhou, L. Zhang, X. Weng, J. Xie, L. Deng, Ultra-broadband absorption in mid-infrared spectrum with graded permittivity metamaterial waveguide structure. Appl. Phys. B **118**(3), 409–415 (2015)
13. F. Monticone, C.A. Valagiannopoulos, A. Alù, Parity-time symmetric nonlocal metasurfaces: all-angle negative refraction and volumetric imaging. Phys. Rev. X **6**(4), 041018 (2016)
14. M. Choi, S.H. Lee, Y. Kim, S.B. Kang, J. Shin, M.H. Kwak, K.-Y. Kang, Y.-H. Lee, N. Park, B. Min, A terahertz metamaterial with unnaturally high refractive index. Nature **470**(7334), 369–373 (2011)
15. X. Yin, Z. Ye, J. Rho, Y. Wang, X. Zhang, Photonic spin hall effect at metasurfaces. Science **339**(6126), 1405–1407 (2013)
16. F. Garwe, C. Rockstuhl, C. Etrich, U. Hübner, U. Bauerschäfer, F. Setzpfandt, M. Augustin, T. Pertsch, A. Tünnermann, F. Lederer, Evaluation of gold nanowire pairs as a potential negative index material. Appl. Phys. B **84**(1–2), 139–148 (2006)
17. C.A. Balanis, *Antenna Theory Analysis and Design*. (Wiley, New York, 2005)
18. H.A. Wheeler, A helical antenna for circular polarization. Proc. IRE **35**(12), 1484–1488 (1947)
19. S.D. Targonski, D.M. Pozar, Design of wideband circularly polarized aperture-coupled microstrip antennas. IEEE Trans. Antennas Propag. **41**(2), 214–220 (1993)
20. M. Fartookzadeh, S.H. Mohseni Armaki, Multi-band conical and inverted conical printed quadrifilar helical antennas with compact feed networks. AEU Int J Electron Commun. **70**(1), 33–39 (2016)
21. J. Huang, C.P. microstrip array with wide axial ratio bandwidth and single feed L.P. elements, in *Antennas and Propagation Society International Symposium*, 1985
22. H. Evans, P. Gale, B. Aljibouri, E.G. Lim, E. Korolkeiwicz, A. Sambell, Application of simulated annealing to design of serial feed sequentially rotated 2 × 2 antenna array. Electron. Lett. **36**(24), 1987 (2000)
23. M. Fartookzadeh, S.H. Mohseni Armaki, Dual-band circularly-polarized monopulse antenna system with single layer patches and separated feed networks. Prog. Electromag. Res. C **55**, 43–52 (2014)
24. M. Fartookzadeh, S.H.M. Armaki, Serial-feed for a circular patch antenna with circular polarization suitable for arrays. Int. J. RF Microw. Comput. Aided Eng. **24**(5), 529–535 (2014)
25. J. Kaschke, M. Wegener, Gold triple-helix mid-infrared metamaterial by STED-inspired laser lithography. Opt. Lett. **40**(17), 3986 (2015)
26. E. Doumanis, G. Goussetis, J.L. Gomez-Tornero, R. Cahill, V. Fusco, Anisotropic impedance surfaces for linear to circular polarization conversion. IEEE Trans. Antennas Propag. **60**(1), 212–219 (2012)
27. J. Wang, Z. Shen, W. Wu, K. Feng, Wideband circular polarizer based on dielectric gratings with periodic parallel strips. Opt. Express **23**(10), 12533 (2015)
28. Y. Liu, S. Xia, H. Shi, A. Zhang, Z. Xu, Dual-band and high-efficiency polarization converter based on metasurfaces at microwave frequencies. Appl. Phys. B **122**(6), 1–8 (2016)
29. Y.Z. Cheng, Y. Nie, Z.Z. Cheng, X. Wang, R.Z. Gong, Asymmetric chiral metamaterial circular polarizer based on twisted split-ring resonator. Appl. Phys. B **116**(1), 129–134 (2014)
30. L. Wu, M. Zhang, B. Zhu, J. Zhao, T. Jiang, Y. Feng, Dual-band asymmetric electromagnetic wave transmission for dual polarizations in chiral metamaterial structure. Appl. Phys. B **117**(2), 527–531 (2014)
31. X. Huang, D. Yang, S. Yu, L. Guo, L. Guo, H. Yang, Dual-band asymmetric transmission of linearly polarized wave using P-shaped metamaterial. Appl. Phys. B **117**(2), 633–638 (2014)
32. M. Fartookzadeh, S.H. Mohseni Armaki, Dual-band reflection-type circular polarizers based on anisotropic impedance surfaces. IEEE Trans. Antennas Propag. **64**(2), 826–830 (2016)
33. D.K. Barton, The 1993 Moscow air show. Microw. J. **37**(5), 24–40 (1994)
34. E.N. Grossman, A. Luukanen, A.J. Miller, Terahertz active direct detection imagers, in *Terahertz for Military and Security Applications II*, Sept, 2004
35. M. Fartookzadeh, S.H. Mohseni Armaki, Enhancement of dual-band reflection-mode circular polarizers using dual-layer rectangular frequency selective surfaces. IEEE Trans. Antennas Propag. **64**, 4570–4574 (2016)

36. D.K. Cheng, *Field and Wave Electromagnetics*. (Pearson Education India, New Delhi, 1989)
37. O. Luukkonen, C. Simovski, G. Granet, G. Goussetis, D. Lioubtchenko, A.V. Raisanen, S.A. Tretyakov, Simple and accurate analytical model of planar grids and high-impedance surfaces comprising metal strips or patches. IEEE Trans. Antennas Propag. **56**(6), 1624–1632 (2008)
38. S. Verma, P. Kumar, Compact triple-band antenna for WiMAX and WLAN applications. Electron. Lett. **50**(7), 484–486 (2014)
39. N. Amani, M. Kamyab, A. Jafargholi, A. Hosseinbeig, J.S. Meiguni, Compact tri-band metamaterial-inspired antenna based on CRLH resonant structures. Electron. Lett. **50**(12), 847–848 (2014)